

Supplementary Information

Programmable topotaxis of magnetic rollers in time-varying fields

Yong Dou, Peter M. Tzelios, Dimitri Livitz, and Kyle J. M. Bishop*

Department of Chemical Engineering, Columbia University, New York, NY, USA

*Address correspondence to kyle.bishop@columbia.edu

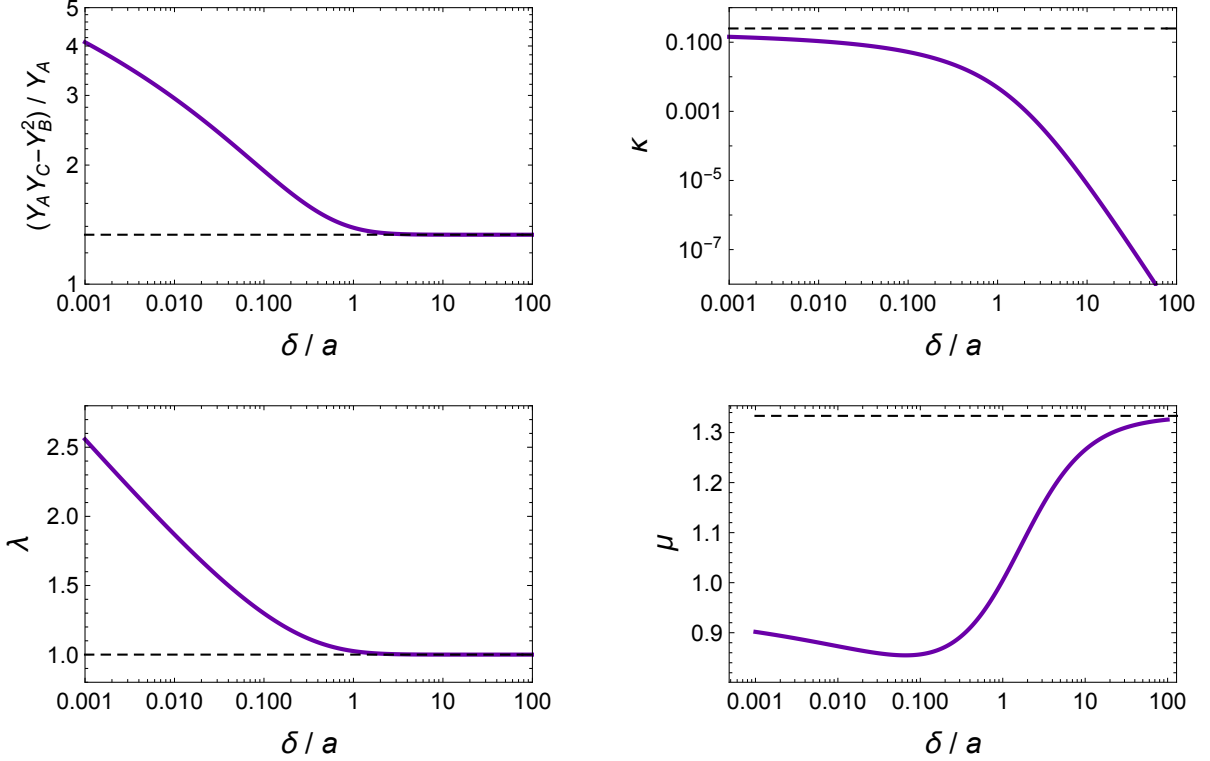


Figure S1: Dimensionless resistance parameters as a function of the surface separation δ scaled by the sphere radius a . (top, left) A torque, $\mathbf{L} = 6\pi\eta a^3\Omega(Y_A Y_C - Y_B^2)/Y_A \mathbf{e}_x$, is required to rotate a force-free sphere with angular velocity, $\mathbf{\Omega} = \Omega \mathbf{e}_x$, above a solid plane normal to \mathbf{e}_z ; the resistance coefficient $(Y_A Y_C - Y_B^2)/Y_A$ approaches $4/3$ for large surface separations $\delta \gg a$. (top, right) A sphere rotating with an angular velocity, $\mathbf{\Omega} = \Omega \mathbf{e}_x$, will translate with a linear velocity, $\mathbf{U} = -\kappa a \Omega \mathbf{e}_y$; the coefficient $\kappa = Y_B/Y_A$ approaches $1/4$ as $\delta \rightarrow 0$, which is four times slower than pure rolling. (bottom, left) The torque required to rotate a sphere with angular speed Ω about the x or y axis is larger by a factor, $\lambda = (Y_A Y_C - Y_B^2)/Y_A X_C$, than that required to rotate the sphere at the same speed about the z axis. (bottom, right) A force, $\mathbf{F} = 6\pi\eta a F(Y_A Y_C - Y_B^2)/Y_C \mathbf{e}_x$, is required to translate a torque-free sphere with linear velocity, $\mathbf{U} = U \mathbf{e}_x$; the parameter, $\mu = Y_C/Y_A$, represents the ratio between the resistance coefficients for rotation and translation parallel to the plane.

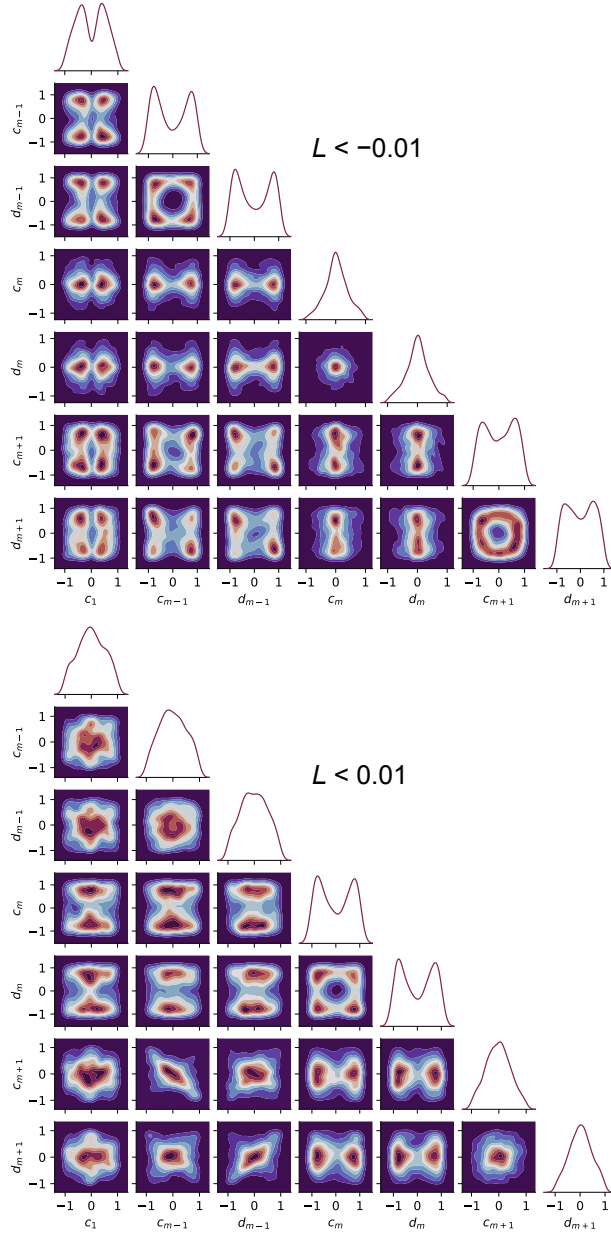


Figure S2: Pairwise distributions among the seven design variables— c_1 , c_{m-1} , d_{m-1} , c_m , d_m , c_{m+1} , and d_{m+1} —for “good” designs satisfying $L < -0.01$ for uphill motion (left) or $L > 0.01$ for downhill motion (right). We used Latin hypercube sampling (LHS) to generate 100,000 candidate designs distributed uniformly on the interval $[-1, 1]$ for each variable. For each candidate, we simulated the resulting particle motion to evaluate the objective function $L(\mathbf{d})$ with rotation order $m = 6$, frequency $\omega = 0.025$, slope $\alpha = 0.2$ radians, and resistance parameters $\kappa = 0.108$ and $\lambda = 1.87$. From these random designs, we identified ca. 1000 “good” designs satisfying the conditions $L < -0.01$ or $L > 0.01$, where the objective function is given by equation (35). The marginal distributions of these designs (plots on the diagonal) and their pairwise correlations (contour plots off the diagonal) reveal strategies for achieving topotaxis. As described in the main text, we used these “good” designs to perform a principle component analysis (PCA) and reduce the dimensionality of the design space without excluding those highest performing designs.

Supplementary Note 1: Data-driven designs with $c_0 \neq 0$

In the main text, we explored the seven dimensional design space—denoted \mathcal{D}_1 —formed by the parameters $c_1, c_{m-1}, d_{m-1}, c_m, d_m, c_{m+1}, d_{m+1}$; static contributions to the field were neglected, $c_0 = 0$. Here, we repeat the design process for a slightly different seven dimensional design space—denoted \mathcal{D}_2 —formed by the parameters $c_0, c_1, c_{m-1}, c_m, d_m, c_{m+1}, d_{m+1}$. Note that we have added c_0 but eliminated d_{m-1} . As the field has rotational symmetry about the z' axis, rotation of the field about that axis by any angle is not important; we can therefore set $d_{m-1} = 0$.

Figure S3 shows the result of the data-driven design process for the new design space. The qualitative trends are the same as those of Figure 4. Reducing the dimensionality of the design space via PCA enables better solutions to be identified more quickly as compared to the full 7-dimensional space. For uphill motion, the best design identified in \mathcal{D}_2 was not as good as that identified in \mathcal{D}_1 : the uphill velocity was $\langle U_y \rangle = 0.0233\omega$ in Figure S3c as compared to $\langle U_y \rangle = 0.0252\omega$ in Figure 4c. Note that the better of these two designs is actually present in both spaces \mathcal{D}_1 and \mathcal{D}_2 but was only discovered during the exploration of \mathcal{D}_1 . By contrast, for downhill motion, improved designs were identified in \mathcal{D}_2 as compared to those identified in \mathcal{D}_1 : the downhill velocity increased from $\langle U_y \rangle = -0.0357\omega$ to $\langle U_y \rangle = -0.0801\omega$. Notably, the best designs identified in \mathcal{D}_2 do not appear to make use of the static component of the magnetic field. Instead, differences between the designs identified in spaces \mathcal{D}_1 and \mathcal{D}_1 reflect the stochastic nature of the design process.

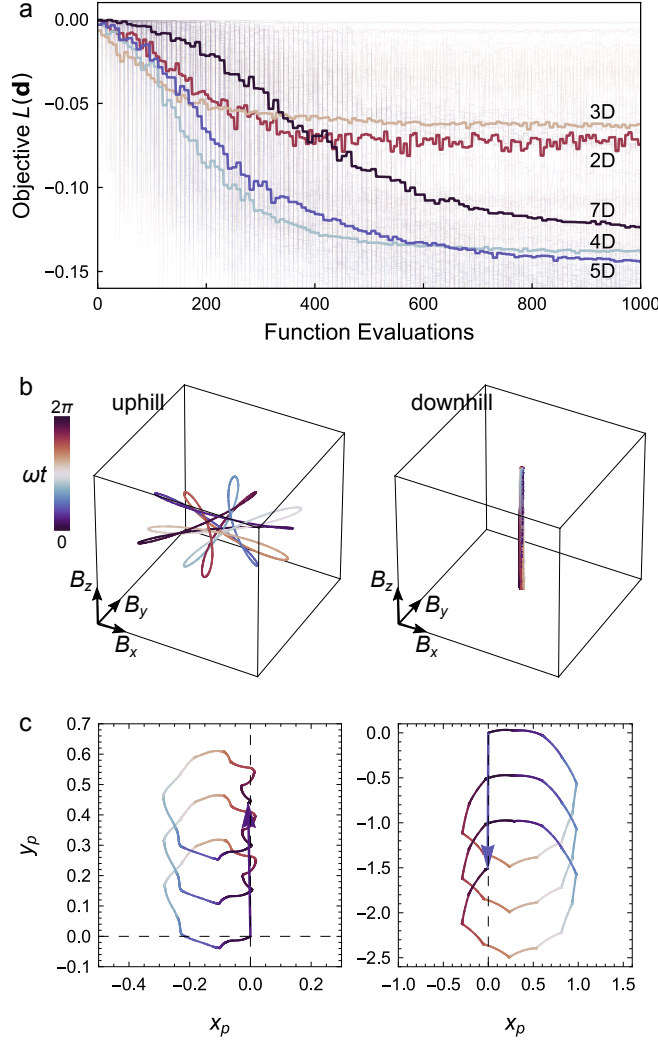


Figure S3: (a) Convergence plot showing the decrease in the objective function $L(\mathbf{d})$ with increasing function evaluations during optimization via CMA-ES. Different colors correspond to design spaces with different numbers of dimensions. For each design space, optimization is initialized from 50 randomly selected designs (light curves); bold curves show the average performance. (b) Two periodic fields $\mathbf{B}'(\omega t)$ identified by the data-driven process to drive particle motion uphill (left) and downhill (right). The uphill field is characterized by design parameters $c_0 = 0.042$, $c_1 = 0.242$, $c_5 = 0.999$, $c_6 = -0.078$, $d_6 = -0.017$, $c_7 = 0.876$, and $d_7 = -0.021$; the downhill by $c_0 = 0$, $c_1 = 0.006$, $c_5 = 0.01$, $c_6 = 0.899$, $d_6 = 0.392$, $c_7 = 0.014$ and $d_7 = 0.025$. (c) Numerically computed particle trajectories in the xy plane over three oscillation cycles using the fields in (b). The drift velocities are $\langle U_y \rangle = 0.0233\omega$ and $\langle U_y \rangle = -0.0801\omega$ for uphill and downhill motion, respectively. In all plots, the symmetry order is $m = 6$; the dimensionless frequency is $\omega = 0.025$; the incline angle is $\alpha = 0.2$ rad; the hydrodynamic parameters are $\lambda = 1.87$ and $\kappa = 0.108$.

Supplementary Note 2: Effects of gravity

If the particle is subject to a constant force \mathbf{F} (scaled by mB_0/a), the Euler angle dynamics presented in the main text is augmented as

$$\dot{\phi} = -\cot \theta (B_x \cos \psi + B_y \sin \psi) - \kappa \csc \theta (F_x \cos \psi + F_y \sin \psi) \quad (1)$$

$$\dot{\theta} = -\cos \theta (B_y \cos \psi - B_x \sin \psi) - B_z \sin \theta + \kappa (F_x \sin \psi - F_y \cos \psi) \quad (2)$$

$$\dot{\psi} = \frac{1}{2} ((1 + \lambda) + (1 - \lambda) \cos 2\theta) \csc \theta (B_x \cos \psi + B_y \sin \psi) + \kappa \cot \theta (F_x \cos \psi + F_y \sin \psi) \quad (3)$$

The particle velocity in the plane of the substrate is given by

$$U_x = \kappa (B_x \cos \theta - B_z \sin \psi \sin \theta) + \mu F_x \quad (4)$$

$$U_y = \kappa (B_y \cos \theta + B_z \cos \psi \sin \theta) + \mu F_y \quad (5)$$

where $\mu = Y_C/Y_A = 0.872$ for a surface separation of $\delta = 0.01a$. We will assume that there is no net force normal to the surface such that there is no motion in the z -direction.

In the main text, we consider the contribution of a gravitational force in equation (5) of the form, $F_y = -F_g \sin \alpha \approx -F_g \alpha$. This force is negligible when

$$F_g \ll \frac{\kappa}{\mu \alpha} \langle B_y \cos \theta + B_z \cos \psi \sin \theta \rangle \quad (6)$$

Using the model-driven design for the uphill migration velocity—equation (29) of the main text—this expression can be written more explicitly as

$$F_g \ll \frac{\kappa C_b b^2 \omega^2}{\mu} \approx 1.5 \times 10^{-3} \quad (7)$$

where the approximate equality assumes a surface separation of $\delta = 0.01a$ and a frequency of $b\omega = 0.3$. Figure S4 shows the computed particle trajectory for the model-driven design for uphill migration in the presence of a weak gravitational force, $F_g = 1.5 \times 10^{-4}$. Under these conditions, the effects of gravity are due primarily to sedimentation and can be superimposed onto the time-averaged dynamics to accurately predict particle motion (dashed black curve). Additional contributions of the force to the orientational dynamics of equations (1)–(3) are negligible.

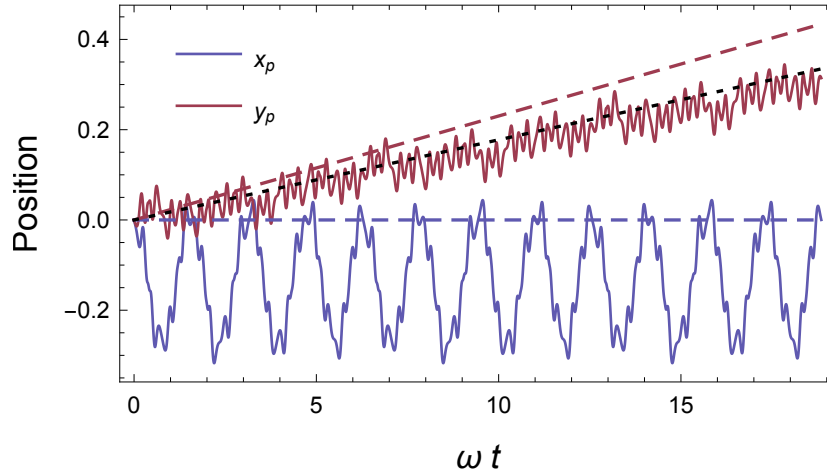


Figure S4: Numerically computed particle trajectories in the xy plane over three oscillation cycles using the model-driven field with $m = 4$ and $b = 40$. In contrast to the results of Figure 3a, this particle is also subject to a gravitational force $F_g = 1.5 \times 10^{-4}$ in the $-\mathbf{e}'_z$ direction. Here, the dimensionless frequency is $\omega = 0.005$; the incline angle is $\alpha = 0.2$ rad; the hydrodynamic parameters are $\lambda = 1.87$, $\kappa = 0.108$, and $\mu = 0.873$ corresponding to a surface separation $\delta = 0.01a$. Particle dynamics computed numerically (solid curves) compare favorably with the time-averaged dynamics (dashed black line) when accounting for sedimentation. The dashed purple line shows the time-averaged dynamics in the absence of gravity.

Supplementary Note 3: Calibration of the Magnetic Coils

In experiments, the magnetic field $\mathbf{B}(t)$ was generated by a triaxial electromagnet powered by three time-dependent currents denoted by the vector $\mathbf{I}(t)$. Within the linear response regime, a harmonic current signal, $\mathbf{I}(t) = \hat{\mathbf{I}}e^{i\omega t}$, creates a magnetic field, $\mathbf{B}(t) = \hat{\mathbf{B}}e^{i\omega t}$, with complex amplitude

$$\hat{\mathbf{B}} = \hat{M}(\omega) \hat{\mathbf{I}} \quad (8)$$

where $\hat{M}(\omega)$ is a complex calibration matrix that depends on the frequency of the applied field. To determine the calibration matrix, we applied a harmonic current signal to each of the three coils (denoted x , y , and z) and measured the resulting magnetic field with a sensor (Ametek MFS-3A, purchased from GMW Associates) positioned at the center of coils. From these data, the components of the calibration matrix were determined by linear regression. We corrected for the ambient magnetic field (ca. 0.05 mT) by taking measurements with the input currents set to zero. For low frequencies $\omega \ll 10$ rad/s, the calibration matrix was real and independent of frequency, $M_0 = \hat{M}(\omega \rightarrow 0)$, with components

$$M_0 = \begin{bmatrix} 4.4 \pm 1.7 \times 10^{-4} & 0.57 \pm 1.5 \times 10^{-4} & -0.057 \pm 1.4 \times 10^{-4} \\ -0.52 \pm 1.5 \times 10^{-4} & 3.9 \pm 1.9 \times 10^{-4} & -0.072 \pm 1.5 \times 10^{-4} \\ -0.093 \pm 1.6 \times 10^{-4} & 0.092 \pm 1.5 \times 10^{-4} & 4.3 \pm 1.9 \times 10^{-4} \end{bmatrix} \text{ mT A}^{-1} \quad (9)$$

where the error-bars correspond to standard errors. In the topotaxis experiments, the desired time-periodic fields $\mathbf{B}(t)$ were generated using the calibrated current signals $\mathbf{I}(t) = M_0^{-1}\mathbf{B}(t)$.

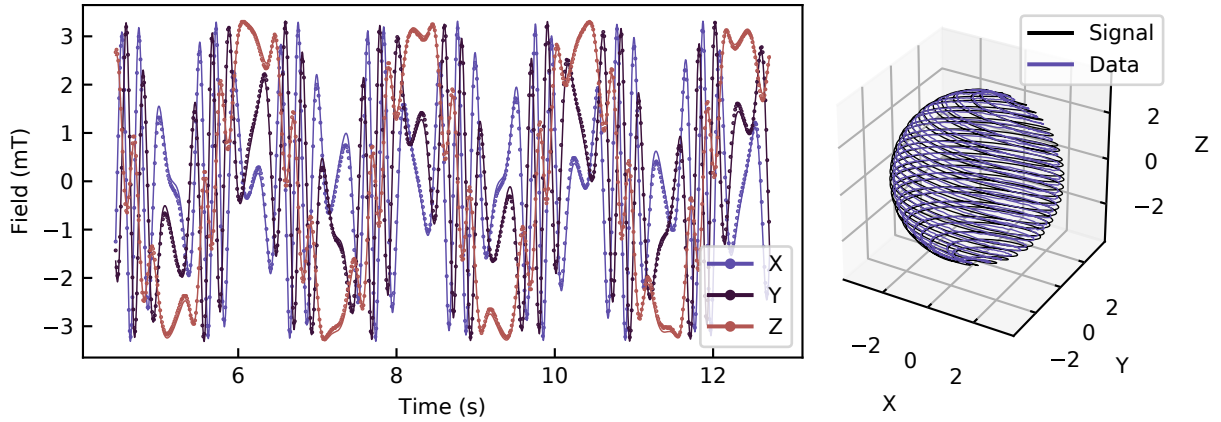


Figure S5: Components of the magnetic field $\mathbf{B}(t)$ during one oscillation cycle of the model-driven design for uphill topotaxis shown in Figure 3a with frequency $\omega = 0.76$ rad/s. After calibration, the measured magnetic field (markers) agrees to within 0.17 mT (6%) with the desired magnetic field (curves). This error is attributed to differences in the position of the sensor between the calibration and measurement experiments, which were performed on different days.

Supplementary Note 4: Magnetic Rolling Experiments

To estimate the magnetic moment of ferromagnetic spheres, we quantified their translational “rolling” motion above a solid planar substrate due to a rotating magnetic field. As illustrated in Figure S6a, a rotating magnetic field in the xz -plane with magnitude B and frequency ω caused the particle to rotate about the y -axis and simultaneously translate in x -direction. Figure S6b shows the measured particle velocity V as a function of the applied frequency. The velocity increases linearly with frequency up to some critical value ω^* , above which it begins to decrease.

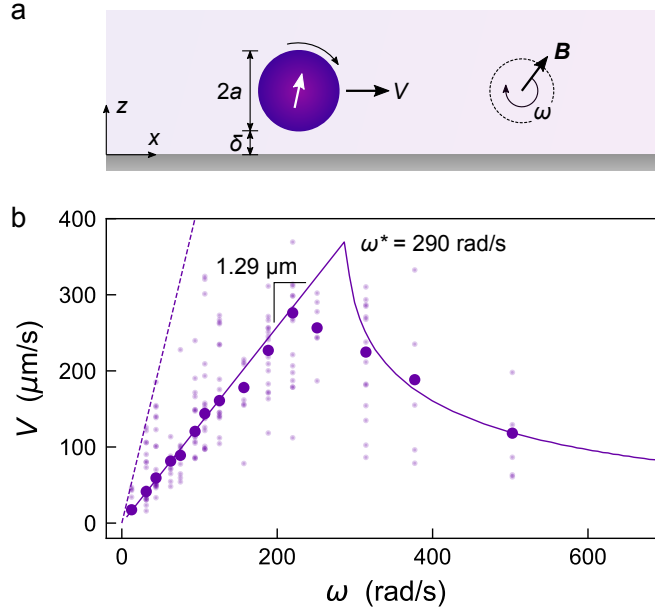


Figure S6: (a) A rotating magnetic field $\mathbf{B}(t)$ drives the rotation and translation of a magnetic Janus particle along a solid wall. (b) Measured particle velocity V as a function of the applied frequency ω (markers). The particle radius was $a = 17 \mu\text{m}$, and the field strength $B_0 = 3.0 \text{ mT}$. Smaller markers denote the velocities of the individual particles; larger markers represent the median velocity. The solid curve shows the predicted velocity of an ideal ferromagnetic sphere with magnetic moment $m = 1.8 \times 10^{-11} \text{ A m}^2$. The dashed curve shows the theoretical bound on hydrodynamic rolling as the surface separation δ approaches zero: $V = a\omega/4$.

This observed behavior is captured quantitatively by a model that accounts for the magnetic and viscous torques acting on the particle and for the hydrodynamic coupling between particle rotation and translation near the solid substrate. Below the critical frequency, the particle’s magnetic moment rotates in lock step with the applied field such that the angular velocity of the particle is equal to that of the field. At low Reynolds numbers, the resulting particle velocity is given by

$$V = \kappa a \omega, \quad (10)$$

where the resistance parameter $\kappa = Y_A/Y_B$ depends on the dimensionless surface separation δ/a . From the experimental data, the fitted slope of the particle velocity versus applied frequency is $1.29 \mu\text{m}$ for $a = 17 \mu\text{m}$. Using these values, eq. (10) implies that the median surface separation is $\delta = 0.041a$. At the critical frequency, the viscous torque on the force-free particle is equal to the

maximum magnetic torque such that

$$6\pi\eta a^3\omega^* \left(\frac{Y_A Y_C - Y_B^2}{Y_A} \right) = mB_0, \quad (11)$$

where the resistance coefficient is $(Y_A Y_C - Y_B^2)/Y_A = 2.30$ for the estimated surface separation $\delta = 0.041a$. Using the known viscosity ($\eta = 8.9 \times 10^{-4}$ Pa s) and field strength ($B_0 = 3.0$ mT), eq. (11) implies that the median magnetic moment is $m \approx 1.8 \times 10^{-11}$ A m².